RSC Advances

ROYAL SOCIETY OF CHEMISTRY

www.rsc.org/advances

TiO_2/Bi_2S_3 core/shell nanowire arrays for photoelectrochemical hydrogen generation

Guanjie Ai, Rong Mo, Qiong Chen, Hang Xu, Sui Yang, Hongxing Li,* and Jianxin Zhong

Hunan Key Laboratory for Micro-Nano Energy Materials and Devices, School of Physics and Optoelectronics, Xiangtan University, Hunan 411105, P. R. China

email:hongxinglee@xtu.edu.cn

TOC Graph

This paper demonstrates the way for construction of nontoxic TiO_2/Bi_2S_3 core/shell NWAs photoanode for PEC hydrogen generation.

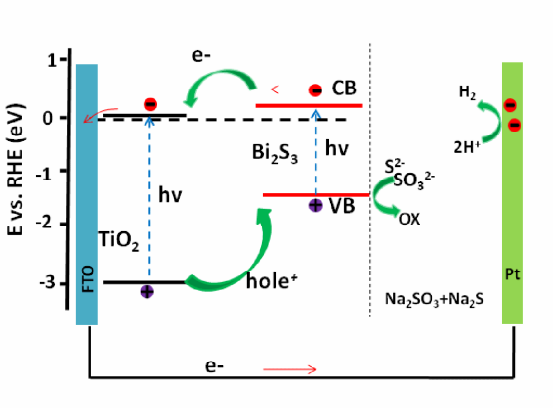

ABSTRACT: A facile and effective procedure for the synthesis of quasi-vertically aligned TiO_2/Bi_2S_3 core/shell nanowire arrays (NWAs) is reported. The nontoxic and earth abundant Bi_2S_3 was assembled onto the hydrothermal pre-grown TiO_2 NWAs *via* successive ionic layer adsorption and reaction (SILAR) method. The morphologies, microstructures, and optical properties of the pristine TiO_2 and composite TiO_2/Bi_2S_3 with different SILAR circles were characterized in detail. For photoelectrochemical (PEC) measurements, the TiO_2/Bi_2S_3 core/shell NWAs exhibited not only an enhanced photocurrent density (2.8 times higher than that of pristine TiO_2), but also a negatively shifted onset potential from 0.067 to -0.072V *vs.* RHE, as compared to the TiO_2. This better PEC performance results from the broadened light absorption and the improved charge carrier separation efficiency. Our results provide a green photoelectrode for PEC hydrogen generation.

Introduction

Since the seminal work of Fujishima and Honda,[1] Titanium dioxide (TiO_2) has been widely investigated as the photoanode material for photoelectrochemical (PEC) hydrogen production owing to its excellent chemical stability, low cost, nontoxicity and environment-friendly feature.[2-7] Among various nanostructured TiO_2, the one dimensional TiO_2 nanowire arrays (NWAs) on transparent FTO substrate has attracted considerable interest due to its facile fabrication, good oriented charge-transport property, and the large specific surfaces for light trapping.[8-14] Despite these advantages, the photoconversion efficiencies of TiO_2 NWAs photoanodes are extremely depressed due to the large energy band gap (3.0 eV for rutile TiO_2).[15, 16] This large energy band gap restricts its solar energy utilization only in the ultraviolet region. Therefore, considerable efforts have been made to enhance their visible light harvesting ability.[17-23] For example, Wang et al. reported that the transition-metal doped TiO_2 NWAs exhibited dramatically improved visible light absorptions and photocatalytic properties in comparison to the pristine TiO_2 samples.[24] Moreover, using morphology controlling strategies to design novel architectures also is explored to the enhanced the light utilization ability of TiO_2, such as the branched TiO_2 nanorod arrays electrode reported by Cho et al. and co-workers.[25]

Sensitizing TiO_2 NWAs with short band gap semiconductors is another approach to extend the working spectrum into the visible range. In this case, the type-II heterostructure NWAs is integrated, and the light absorption can be extended by the narrower band gap sensitizers. In addition, the charge separation efficiency can also be largely improved due to the build-in space electric field. The conventional II-VI semiconductors such as CdS and CdSe, have exhibited considerable PEC performance improvement as sensitizers for TiO_2 NWAs. However, their fatal toxicity is a worrying issue when used for practical applications. Recently, Bi_2S_3 has been emerging to be an effective, inexpensive and environmentally friendly light absorber material for wide band gap semiconductors.[26] For example, Gao et al. reported the Bi_2S_3-coated $BiVO_4$ discoids by in situ transform the surface $BiVO_4$ into Bi_2S_3.[27] The

heterostructured $BiVO_4/Bi_2S_3$ exhibited superior photocurrent response and photocatalytic activity for the reduction of Cr^{VI} under visible light illumination. Besides, Lin et al. demonstrated that the Bi_2S_3 quantum dots sensitized SnO_2 porous film photoelectrode achieved a high photocurrent density of 0.9 mA cm^{2-} under 0.109 sun illumination.[28] Also, there has been several reports on the hybridization of TiO_2 with Bi_2S_3 for PEC application.[29-31] For example, Zumeta-Dube et al. reported the Bi_2S_3 quantum dots (QDs) sensitized TiO_2-P25 with PEC conversion efficiency of 0.84%.[32]

In this paper, we report the heterostructured TiO_2/Bi_2S_3 core/shell NWAs synthesized by successive ionic layer adsorption and reaction of Bi_2S_3 onto the pre-grown TiO_2 NWAs for solar-light-driven PEC hydrogen generation. This hybrid TiO_2/Bi_2S_3 outstands itself from the early reported TiO_2/Bi_2S_3 composites by its one dimensional morphology. Comparing to the conventional II-VI semiconductors (such as CdS and CdSe) sensitized TiO_2, this composite TiO_2/Bi_2S_3 is environment-friendly and low-cost. The as-obtained photoanode exhibits strong absorption in the visible spectrum up to 800 nm. With light illumination, the optimized photoanode yields a photocurrent of ~0.97 mA/cm^2 at 0.2671 V *vs.* RHE, which is 2.8 times of that of pure TiO_2 samples. Moreover, the TiO_2/Bi_2S_3 composite photoanodes induce a cathodic shift of the onset potential. The excellent PEC properties of our photoanodes show that the hybridization of Bi_2S_3 on the TiO_2 NWAs has potential applications in QDs sensitized solar cells, PEC hydrogen generation and photocatalysis.

Experimental details

Preparation of TiO_2 NWAs by hydrothermal method

TiO_2 NWAs were grown onto fluorine-doped tin oxide (FTO) substrates using a hydrothermal method reported previously.[33] Briefly, 0.45 ml titanium n-butoxide and 0.6 g NaCl were added into the 30 ml diluted hydrochloric acid (mass fraction 18.25-19%) and stirred until the mixture became clear. After that, the above precursor was transferred into a 100 ml Teflon-lined stainless steel autoclave in which the FTO substrates were placed with an angle against the in-wall with the conductive side

facing down. The hydrothermal process was conducted in an electric oven at 150 ℃ for 8 h. After cooling, the resultant samples were removed and rinsed with water to get rid of any residual reactants and dried in air at 80 ℃.

Preparation of Bi_2S_3-sensitized TiO_2 NWAs by SILAR

For Bi_2S_3 sensitization, the as-synthesized TiO_2 NWAs were successively immersed into two different solutions for 1 min each, first in 0.05 M $Bi(NO_3)_3$ solution and then in 0.1 M Na_2S in aqueous solution. The $Bi(NO_3)_3$ solution was ultrasonic dissolved with the pH adjusted to 1~2 by concentrated nitric acid. Following each immersion, the electrodes were rinsed with deionized water and dried with a nitrogen stream to remove excess precursors before the next dipping. The two-step dipping procedure was called one SILAR cycle. Sample that went through *n* SILAR cycles is referred to as TiO_2/ Bi_2S_3(*n*). Finally, the as-prepared TiO_2/ Bi_2S_3 hybrid electrodes and the bare TiO_2 electrode were annealed at 250 ℃ in Ar atmosphere for 1 hour.

Structural and optical characterizations

The morphology and microstructure of the samples were characterized using the field emission scanning electron microscope (NOVA NANOSEM 450, FEI, USA) equipped with an energy-dispersive X-ray spectroscopy (EDS) and transmission electron microscopy (TEM, JEM2010-HR, 200 KV). Raman spectra of the as-obtained samples were recorded on a Renishaw InVia system with a laser operating at λ=532 nm as the excitation source. The crystal structure was characterized by a Rigaku Dmax 2500 X-ray diffractometer with Cu K_α radiation. The light absorption was recorded by UV-vis spectrophotometer (UV-2500, Shimadzu, Japan).

PEC measurements

The PEC properties of the photoelectrodes were studied on an electrochemical workstation (CH Instruments, model CHI660E). The three-electrode system was used with the TiO_2 or TiO_2/Bi_2S_3 NWAs on FTO substrates as the working electrodes, a Pt foil as counter electrode and Ag/AgCl as reference electrode. A mixture aqueous solution of 0.24 M Na_2S and 0.35 M Na_2SO_3 (pH=11.5) was used as the electrolyte and sacrificial reagent for all PEC measurements. A 150 W Xe lamp was used as the light source. Before test, the incident light intensity was calibrated to 100 mW cm^{2-}

with a digital power meter. The photocurrent densities *vs.* measured potential (*i*−*v* curves) measurements were carried out at a scan rate of 25 mV s^{-1}. The *i*−*t* curves were measured with a chopped light illumination at -0.6 V bias *vs.* Ag/AgCl. Electrochemical impedance spectroscopy (EIS) was measured under light at the open-circuit potential, with frequency range from 0.01 Hz to 100 kHz and the modulation amplitude of 5 mV. Mott−Schottky plots were measured in the dark at an AC frequency of 1.0 kHz. For all PEC measurements, the active area of the working electrodes was strictly kept within 1 cm^2. Hereafter, the electrode potential versus the Ag/AgCl is converted to the reversible hydrogen electrode (RHE) potential according to the Nernst equation[34]

$$E_{RHE} = E_{Ag/AgCl} + 0.059\,pH + E^{\theta}_{Ag/AgCl}$$

where E_{RHE} is the converted potential *vs.* RHE, $E^{\theta}_{Ag/AgCl}$ = 0.1976 V at 25 °C, and $E_{Ag/AgCl}$ is the experimental potential measured against the Ag/AgCl reference electrode.

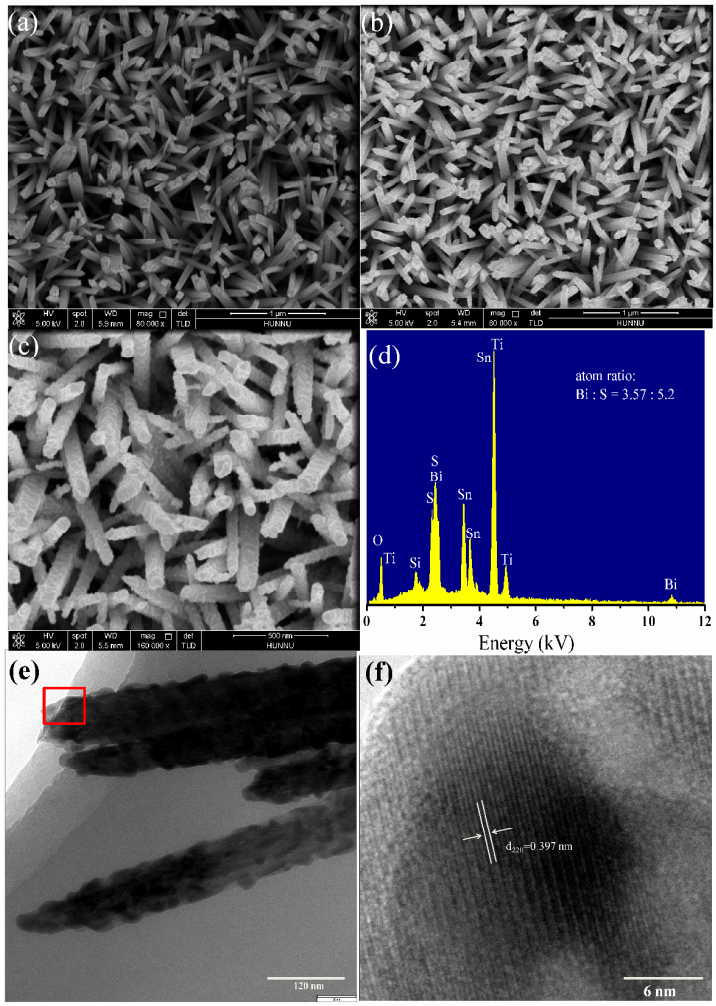

Fig. 1 SEM images of bareTiO_2 (a) and TiO_2/Bi_2S_3(20) (b) NWAs, respectively. (c) Magnified SEM image of TiO_2/Bi_2S_3(20) NWAs. (d) EDS of TiO_2/Bi_2S_3(20) NWAs. TEM (e) and HRTEM (f) images of TiO_2/Bi_2S_3(20) NWAs, respectively.

Results and discussion

Fig. 1a shows the typical top view SEM image of the bare TiO_2 NWAs. As seen, the TiO_2 NWAs are uniformly grown on the entire substrate with diameter around 75 nm, and the rod exhibits a regular tetragonal growth. For composite photoanodes, we synthesized three TiO_2/Bi_2S_3 core/shell NWAs samples with 10, 20 and 30 SILAR circles, and referred to them as TiO_2/Bi_2S_3(10), TiO_2/Bi_2S_3(20) and TiO_2/Bi_2S_3(30), respectively. After the deposition of Bi_2S_3 layer, the surfaces of the TiO_2 NW become rough. Fig. 1b shows the low magnification SEM image of the TiO_2/Bi_2S_3 NWAs

with 20 SILAR deposition circles. Compare to Fig. 1a, Bi_2S_3 modified TiO_2 shows similar NWA feature but the image is slightly bright, suggest that the Bi_2S_3 sensitizers make the surfaces more conductive. Fig. 1c shows the morphology of the TiO_2/Bi_2S_3(20) sample under higher magnification. As can be seen from Fig. 1c, Bi_2S_3 is uniformly deposited onto the TiO_2 NW surfaces and the diameter TiO_2/Bi_2S_3(20) is increased to approximately 100 nm. Hence, the Bi_2S_3 deposition thickness is approximately 13 nm. These observations indicate the successful synthesis of core-shell TiO_2/Bi_2S_3 NWA hetrostructures. The morphologies of the composite TiO_2/Bi_2S_3 NWAs with different SILAR circles are also exhibited in Fig. S1(a-c) (see supporting information). With increasing of SILAR circles, a larger diameter and rougher surface of TiO_2/Bi_2S_3 composite NWAs are displayed. In addition, some overdosed Bi_2S_3 nanoparticles are blocked at the interspaces of NWAs when the SILAR circles increased up to 30. This overloading of Bi_2S_3 is detrimental for PEC performance of TiO_2/Bi_2S_3 photoelectrode which will be discussed later. The TEM images of the Fig. S1(e-f) gives a more straight-forward observation of the thickness of the Bi_2S_3 layer with different SILAR circles, from which we can also reckon the particle-initiated growth behavior of the Bi_2S_3 layer. When the SILAR circle is 10, only a few separated Bi_2S_3 particles are decorated on the TiO_2 NW, the average diameter of the Bi_2S_3 particles is 20 nm. Increasing the SILAR circle up to 20, more Bi_2S_3 particles are loaded on the TiO_2 NW (dark dot in Fig. S1e), and the particles tend to interlink to each other resulting in an overall covering of the TiO_2 NW surface. The 30 SILAR circles make a ~25 nm thickness shell on the TiO_2 NW (inset in Fig. S1f), and the particle-stacked Bi_2S_3 shell can be directly seen. Fig. 1d displays the EDS spectrum of the TiO_2/Bi_2S_3 NWAs, the atomic ratio of Bi:S is found to be ~2:3, showing that the samples are in even stoichiometric. The other peaks of Ti, Si, Sn, Ca, and O are attributed to the chemical components of TiO_2 NWAs and the FTO glass substrate. Fig. 1e shows the TEM image of TiO_2/Bi_2S_3(20) core/shell NWs, it can be observed that the 1D TiO_2 NW is sheathed by the Bi_2S_3 nanoparticles throughout the length. Fig. 1f is the HRTEM image taken from the red square in Fig. 1e. The observed interplanar spacing of 0.397 nm corresponds to the (220) plane of

orthorhombic Bi_2S_3, which is agree with the result observed by XRD below.

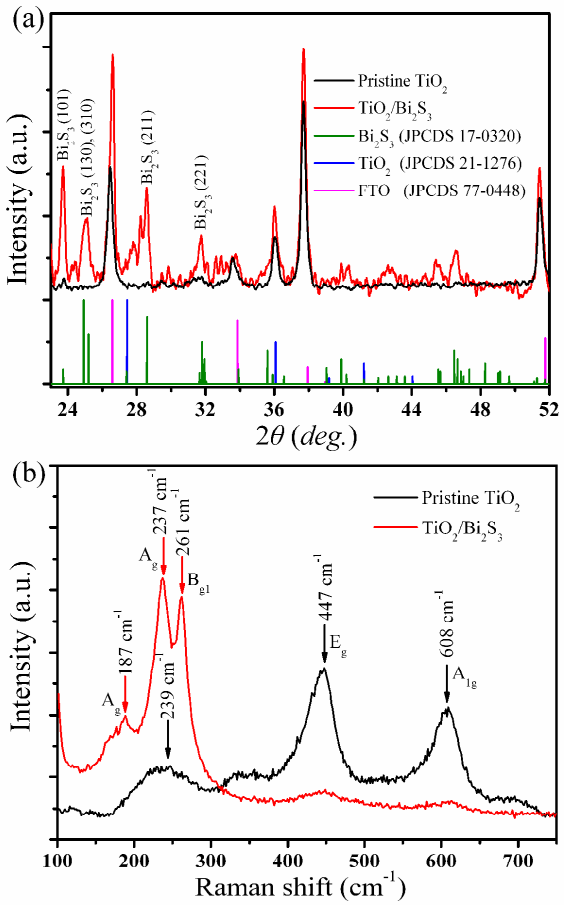

Fig. 2 (a) XRD patterns and (b) Raman scattering spectra of the pristine TiO_2 and composite TiO_2/Bi_2S_3 NWAs on FTO substrates.

The XRD patterns of the as-obtained samples were collected to character their crystallographic phases (Fig. 2a). The pattern of the pristine TiO_2 NWAs (black line in Fig. 2a) reveal that the TiO_2 have a rutile structure (JPCDS 21-1276). Apart from the peaks of TiO_2 and FTO substrate (JPCDS 77-0448), the additional diffraction peaks (red line in Fig. 2a) can be readily indexed to the orthorhombic phase of Bi_2S_3 (JCPDS 17-0320) for TiO_2/Bi_2S_3 composite electrode. The main peaks at 2θ of 23.7, 24.9, 25.2, 28.6, and 31.76 are corresponding to the (101), (130), (310), (211) and (221) planes of orthorhombic Bi_2S_3, respectively. Fig. 2b shows the Raman spectra of the TiO_2 and TiO_2/Bi_2S_3 NWAs photoanodes. The pristine TiO_2 exhibits two sharp peaks at 447 and 608 cm^{-1}, which can be attributed to the E_g and A_{1g} mode in rutile

TiO_2 as reported by Porto et al.[35] The broad peak at 239 cm^{-1} is of a complex nature, which is relevant to the second-order scattering and disorder effects. The coating of Bi_2S_3 layer weakens characteristic peaks of the TiO_2 and three new peaks at 237 and 261 cm^{-1} and 187 cm^{-1} are emerged. The added peaks can be attributed to the A_g, B_{g1} and A_g mode of the Bi_2S_3,[36, 37] which indicates the crystalline character of Bi_2S_3 layer in the TiO_2/Bi_2S_3 composite NWAs.

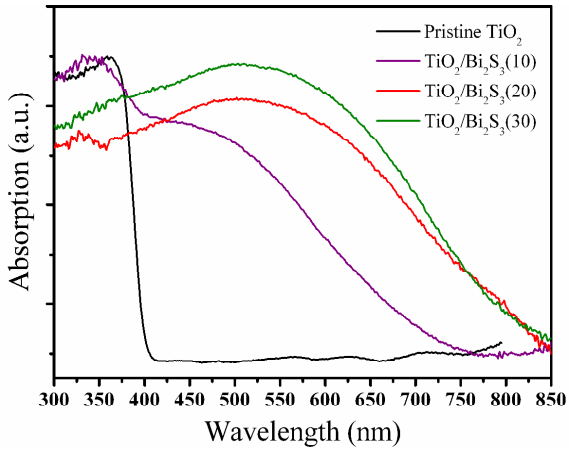

Fig. 3 Normalized UV-vis absorption spectra of TiO_2 and TiO_2/Bi_2S_3 core/shell NWAs on FTO substrates.

The optical absorption properties of the TiO_2 and TiO_2/Bi_2S_3 were characterized by absorption spectra, as shown in Fig. 3. We can see that the absorption wavelength of TiO_2 NWAs is less than 410 nm. In the case of the composite TiO_2/Bi_2S_3 NWAs, its absorption extends to cover the whole visible light range and even beyond 800 nm. In addition, UV-vis absorption spectra show that as the SILAR deposition circle increases the light absorption ability also increases. The relationship between the incident photon energy and the absorption coefficient is given by the following equation: $(\alpha hv)^2 = A(hv - E_g)$, where α , h, v and E_g are the optical absorption coefficient, Planck constant, the photon frequency and band gap of semiconductor, respectively. A is a constant. The band-gap values of TiO_2 and $TiO_2/Bi_2S_3(20)$ are derived to be 3.02 and 1.6 eV, respectively. This enhancement of light trapping effect for $TiO_2/Bi_2S_3(20)$ is beneficial for the PEC hydrogen generation application.

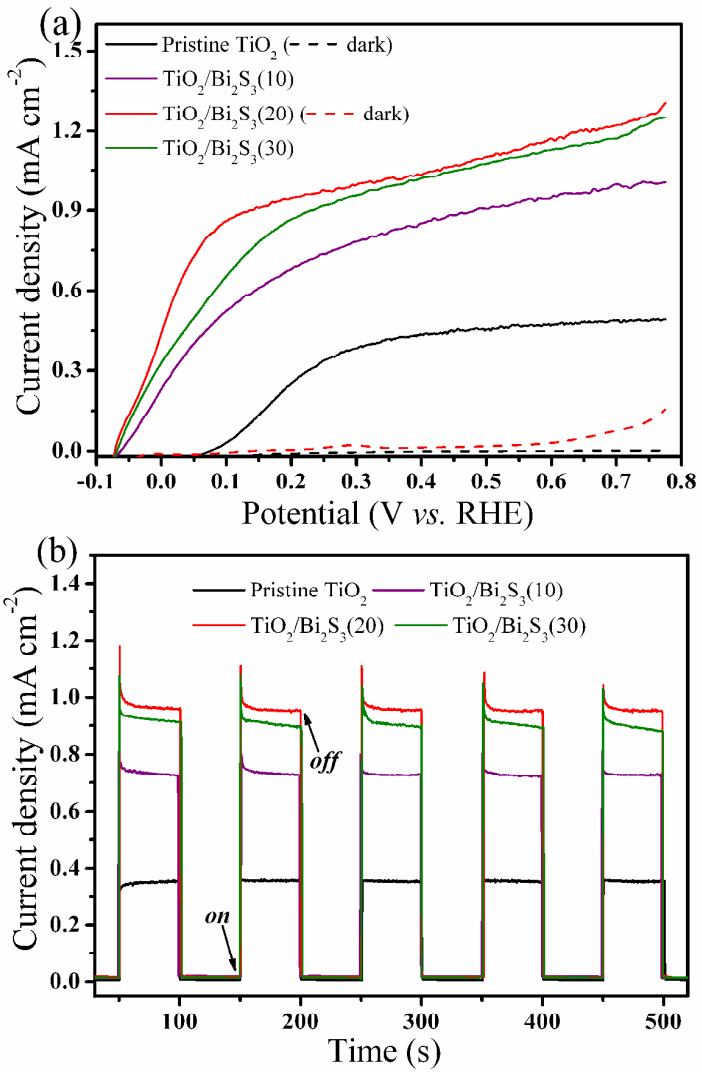

Fig.4 (a) *i-v* curves under AM 1.5G in the dark and at 100 mW cm^{2-} illumination for pristine TiO_2 NWAs and TiO_2/Bi_2S_3 core/shell NWAs with different circles SILAR. (b) Amperometric *i-t* curves of the TiO_2/Bi_2S_3 (10, 20, 30) core/shell NWAs at 0.2761 V versus RHE with light on/off cycles.

To evaluate the Bi_2S_3 sensitization effect on PEC performance of TiO_2, Fig. 4a shows the *i-v* curves of the bare TiO_2 and the TiO_2/Bi_2S_3 core/shell NWAs with 10, 20 and 30 SILAR circles. By analyzing the experimental data in Fig. 4a, three conclusions can be reached. First, for all of the TiO_2/Bi_2S_3 NWAs photoanodes, the saturate photocurrent densities are much higher than that of the pristine TiO_2. The TiO_2/Bi_2S_3(20) sample achieved a value of 0.98 mA/cm^2 at 0.2671 V *vs.* RHE (-0.6 V

vs. Ag/AgCl), which is higher than that of the bare TiO_2 (0.35 mA cm^{2-}) and other composite photoanodes (0.8 mA cm^{2-} for TiO_2/Bi_2S_3(10) and 0.95 mA/cm^2 for TiO_2/Bi_2S_3(30)). It confirms that the coating of Bi_2S_3 is a simple but effective method for enhancing the PEC performance of TiO_2. Second, as compared to TiO_2, the onset potential of TiO_2/Bi_2S_3 is much negatively shifted and leads to the photocurrent saturation at a more negative potential. Typically, the photocurrent increases from the onset potential around -0.072 V *vs.* RHE and approaches a plateau at 0.05 V *vs.* RHE for TiO_2/Bi_2S_3(20) sample, whereas the photocurrent plateau in the bare TiO_2 photoanode is 0.3 V *vs.* RHE. Achieving the saturated photocurrent level at a more negative potential is significantly important because it reduces the applied external bias, and thus increases the overall efficiency of the PEC cells.[22] Third, the TiO_2/Bi_2S_3(20) overmatches the one with 10 or 30 SILAR circles deposition. As the Bi_2S_3 deposition increasing, the light absorption of TiO_2/Bi_2S_3 is also increased (see Fig. 3). However, too much Bi_2S_3 deposition blocks the porous structure of the electrodes (see SEM images of Fig. S1 in supporting information) and lengthens the electron diffusion path from Bi_2S_3 to TiO_2. In this case, a more positive external bias is needed to separate the photo-induced charge efficiently for TiO_2/Bi_2S_3(30), which can explain the smaller photocurrent between 0 and 0.3 V *vs.* RHE but similar photocurrent when the potential exceeds 0.35 V *vs.* RHE in comparison with TiO_2/Bi_2S_3(20). Fig. 4b shows the *i-t* curves of the TiO_2 and the TiO_2/Bi_2S_3 (20) core/shell NWAs photoelectrodes at 0.2671 bias *vs.* RHE under chopped light irradiation. Upon illumination, the photocurrent of TiO_2/Bi_2S_3 (20) flashily rise to a high level, and decay to a relatively steady-state after a few second, displaying a series of spikes in the photoresponse. This behavior might be attributed to the charge carrier accumulation at the electrode-electrolyte interface due to the slow oxygen evolution kinetics or oxidization of trap states on the surface and in the bulk by charge carriers.[38] And when the light is cut off, the photocurrent densities drop to nearly zero instantaneously. Such fast rise and fall of the photocurrents indicates that carrier transport in the heterojunction material proceeds very quickly.

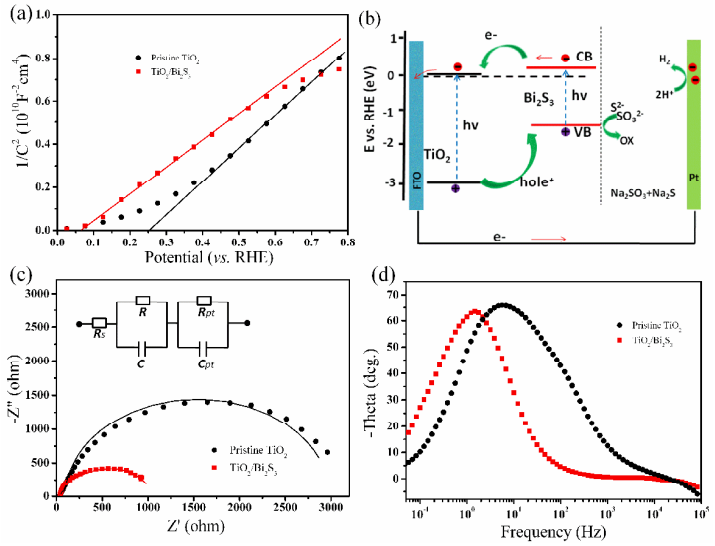

Fig. 5 (a) Mott-Schottky plots of pristine TiO_2 and TiO_2/Bi_2S_3(20) core/shell NWAs. (b) Schematic of energy band level aliment and carrier transferring mechanism in TiO_2/Bi_2S_3 core/shell NWAs. (c) Nyquist plots and (d) Bode plots of the impedance spectra measured at open circuit condition under 1 sun illumination.

Fig. 5a shows the Mott-Schottky (M-S) plots, in which the flat band potential at the electrode/electrolyte interface can be estimated by the M-S equation[39]

$$1/C^2 = (2/\varepsilon\varepsilon_0 e N_d\, A^2)[(V - V_{FB}) - kT/e_0]$$

where C is the specific capacity, ε is the dielectric constant of Bi_2S_3 or TiO_2, ε_o is the electric permittivity of vacuum, N_d is the carrier density, A is the area, V is the applied potential, V_{FB} is the flat band potential, k is the Boltzmann constant, T is the absolute temperature, and e_0 is the electron charge. The V_{FB} values of the TiO_2/Bi_2S_3 and TiO_2 NWAs are determined to be 0.07 V and 0.26 V *vs.* RHE by extrapolating the X-intercepts of the linear region in the M−S plot, respectively. Such a negative shift of the flat band for the TiO_2/Bi_2S_3 electrode suggests a higher carrier concentration and lower charge recombination in the TiO_2/Bi_2S_3 electrode in comparison with the pristine TiO_2. In addition, the positive slope indicates that the TiO_2/Bi_2S_3 NWA is an n-type semiconductor. The TiO_2/Bi_2S_3 shows substantially smaller M-S plot slope compared to the TiO_2, suggesting an increase of donor density in the TiO_2/Bi_2S_3.[9] Using the resulted V_{FB} and band gap values of the TiO_2/Bi_2S_3 and TiO_2, the energy

band level aliments can be estimated as displayed in Fig. 5b.[40] The charge transfer and hydrogen production mechanism in the TiO_2/Bi_2S_3 PEC cell is proposed. When the TiO_2/Bi_2S_3 heterojunction is irradiated by solar light, electrons are excited to the conduction band (CB) of Bi_2S_3 and TiO_2. Subsequently, electrons migrate from Bi_2S_3 to TiO_2 and finally to the counter electrode to produce H_2. At the same time, the holes are transported to the valence band (VB) of Bi_2S_3 and then scavenged by the sacrificial reagents at the electrode/electrolyte interface. Thus, the photogenerated charge separation efficiency is improved because of the formation of type-II heterojunction interface in the TiO_2/Bi_2S_3 electrode, which is also responsible for its high photocurrent density.

To further examine the intrinsic electronic properties of the TiO_2/Bi_2S_3 NWAs, the EIS were collected and shown in Fig. 5c. Normally, the smaller the radius in Nyquist plot, the lower the charge transfer impedance at the electrode-electrolyte interface for corresponding electrode.[41] The TiO_2/Bi_2S_3 composite electrodes represent much smaller radii than the pristine TiO_2 electrode, implying its more effective charge carrier separations compared to the pristine TiO_2. The inset in the Nyquist plots is the equivalent circuit model of the PEC cell, where the R_s is the series resistance of the electrochemical device, R and C represent the resistance and capacitance of space charge region, respectively, including charge transfer across the FTO/TiO_2-Bi_2S_3 interface and the TiO_2-Bi_2S_3/electrolyte interface, R_{Pt} and C_{Pt} are the resistance and capacitance of the Pt cathode, respectively. By fitting the experimental data (dot points) into solid line using the equivalent circuit model, a more quantitative approach to compare the interface charge transfer impedance of TiO_2 and TiO_2/Bi_2S_3 is reached. As a result, the determined value of R is 3270 and 735 Ω for pristine TiO_2 and composite TiO_2/Bi_2S_3 photoelectrodes, respectively. Correspondingly, the TiO_2/Bi_2S_3 heterojunction shows a lower characteristic peak frequency in the Bode phase plot in Fig. 5d, implying the longer electron lifetime than that of the pristine TiO_2 electrode.[42] The enhanced charge separation and prolonged electron lifetime in the TiO_2/Bi_2S_3 composite is also responsible for the improved PEC performance for TiO_2.

Conclutions

In summary, we have successfully synthesized the TiO_2/Bi_2S_3 core/shell NWAs as photoelectrode for PEC hydrogen generation. The coating of Bi_2S_3 layer achieves a remarkable enhancement of photocurrent density in the TiO_2 NWAs photoanode. Moreover, the onset potential of the composite photoanode is also largely shifted to a negative direction. The broadened light absorption and improved charge carrier separation efficiency in the type-II TiO_2/Bi_2S_3 core/shell NWAs are responsible for the PEC performance enhancement. The present work provides a new photoelectrode with non-toxicity, low cost and easy fabrication, which may have potential application in PEC hydrogen generation and photocatalysis.

Acknowledgements

We thank the financial support of the National Natural Science Foundation of China (Grant no. 51202208, 51172191, and 11274264), The Project Supported by Scientific Research Fund of Hunan Provincial Education Department (Grant no. 12B129), National Basic Research Program of China (no. 2012CB921303) and the Program for Changjiang Scholars and Innovative Research Team in University (IRT13093).

References:

1 A. Fujishima and K. Honda, *Nature*, 1972, **238**, 37-38.

2 S. U. M. Khan, *Science*, 2002, **297**, 2243-2245.

3 I. Mora-Seró, T. L. Villarreal, J. Bisquert, Á. Pitarch, R. Gómez and P. Salvador, *J. P. C. B*, 2005, **109**, 3371-3380.

4 P. R. Mishra, P. K. Shukla and O. N. Srivastava, *Int. J. Hydrogen Energ.*, 2007, **32**, 1680-1685.

5 J. H. Pan, X. Z. Wang, Q. Huang, C. Shen, Z. Y. Koh, Q. Wang, A. Engel and D. W. Bahnemann, *Adv. Funct. Mater.*, 2014, **24**, 95-104.

6 H. Cui, W. Zhao, C. Yang, H. Yin, T. Lin, Y. Shan, Y. Xie, H. Gu and F. Huang, *J. Mater. Chem. A*, 2014, **2**, 8612.

7 Q. Dong, H. Yu, Z. Jiao, G. Lu and Y. Bi, *RSC Advances*, 2014, **4**, 59114-59117.

8 Q. Dong, H. Yu, Z. Jiao, G. Lu and Y. Bi, *RSC Advances*, 2014, **4**, 59114.

9 Q. Kang, J. Cao, Y. Zhang, L. Liu, H. Xu and J. Ye, *J. Mater. Chem. A*, 2013, **1**, 5766.

10 W. Wu, B. Lei, H. Rao, Y. Xu, Y. Wang, C. Su and D. Kuang, *Sci. Rep.*, 2013, **3**. No. 1352, DOI: 10.1038/srep01352.

11 P. Roy, D. Kim, K. Lee, E. Spiecker and P. Schmuki, *Nanoscale*, 2010, **2**, 45.

12 B. Liu and E. S. Aydil, *J. Am. Chem. Soc.*, 2009, **131**, 3985-3990.

13 A. Wolcott, W. A. Smith, T. R. Kuykendall, Y. Zhao and J. Z. Zhang, *Small*, 2009, **5**, 104-111.

14 K. Hara, K. Sayama, H. Arakawa, Y. Ohga, A. Shinpo and S. Suga, *Chem. Commun.*, 2001, 569-570.

15 N. Jain, Y. Zhu, D. Maurya, R. Varghese, S. Priya and M. K. Hudait, *J. Appl. Phys.*, 2014, **115**, 24303.

16 D. O. Scanlon, C. W. Dunnill, J. Buckeridge, S. A. Shevlin, A. J. Logsdail, S. M. Woodley, C. R. A. Catlow, M. J. Powell, R. G. Palgrave, I. P. Parkin, G. W. Watson, T. W. Keal, P. Sherwood, A. Walsh and A. A. Sokol, *Nature Materials*, 2013, **12**, 798-801.

17 Q. Liu, H. Lu, Z. Shi, F. Wu, J. Guo, K. Deng and L. Li, *ACS Appl. Mater. Interfaces*, 2014, **6**, 17200-17207.

18 M. Khan, P. Jiang, J. Li and W. Cao, *J. Appl. Phys.*, 2014, **115**, 153103.

19 C. Dette, M. A. Pérez-Osorio, C. S. Kley, P. Punke, C. E. Patrick, P. Jacobson, F. Giustino, S. J. Jung and K. Kern, *Nano Lett.*, 2014, **14**, 6533-6538.

20 Y. Li, W. Wu, P. Dai, L. Zhang, Z. Sun, G. Li, M. Wu, X. Chen and C. Chen, *RSC advances*, 2014, **4**, 23831.

21 S. Kurian, H. Seo and H. Jeon, *J. Phys. Chem. C*, 2013, **117**, 16811-16819.

22 G. Wang, H. Wang, Y. Ling, Y. Tang, X. Yang, R. C. Fitzmorris, C. Wang, J. Z. Zhang and Y. Li, *Nano Lett.*, 2011, **11**, 3026-3033.

23 B. Liu, H. M. Chen, C. Liu, S. C. Andrews, C. Hahn and P. Yang, *J. Am. Chem. Soc.*, 2013, **135**, 9995-9998.

24 C. Wang, Z. Chen, H. Jin, C. Cao, J. Li and Z. Mi, *J. Mater. Chem. A*, 2014, **2**, 17820-17827.

25 I. S. Cho, Z. Chen, A. J. Forman, D. R. Kim, P. M. Rao, T. F. Jaramillo and X. Zheng, *Nano Lett.*, 2011, **11**, 4978-4984.

26 T. Wu, X. Zhou, H. Zhang and X. Zhong, *Nano Research*, 2010, **3**, 379-386.

27 X. Gao, H. B. Wu, L. Zheng, Y. Zhong, Y. Hu and X. W. D. Lou, *Angew. Chem., Int. Ed.*, 2014, **53**, 5917-5921.

28 Y. C. Lin and M. W. Lee, *J. Electrochem. Soc.*, 2013, **161**, H1-H5.

29 J. Kim and M. Kang, *Int. J. Hydrogen Energ.*, 2012, **37**, 8249-8256.

30 R. Brahimi, Y. Bessekhouad, A. Bouguelia and M. Trari, *Catal. Today*, 2007, **122**, 62-65.

31 L. M. Peter, K. G. U. Wijayantha, D. J. Riley and J. P. Waggett, *J. Phys. Chem. B*, 2003, **107**, 8378-8381.

32 I. Zumeta-Dubé, V. Ruiz-Ruiz, D. Díaz, S. Rodil-Posadas and A. Zeinert, *J. Phys. Chem. C*, 2014, **118**, 11495-11504.

33 G. Ai, R. Mo, H. Xu, Q. Chen, S. Yang, H. Li and J. Zhong, *J. Appl. Phys.*, 2014, **116**, 174306.

34 M. Gratzel, *Nature*, 2001, **414**, 338-344.

35 S. P. S. PoRTQ, P. A. FLEURY and T. C. DAMEN, *Phys. Rev.*, 1967, **154**, 522.

36 T. Lutz, A. MacLachlan, A. Sudlow, J. Nelson, M. S. Hill, K. C. Molloy and S. A. Haque, *Phys. Chem. Chem. Phys.*, 2012, **14**, 16192.

37 Y. Zhao, K. T. E. Chua, C. K. Gan, J. Zhang, B. Peng, Z. Peng and X. Qihua, *Phys. Rev. B*, 2011, **84**, 205330.

38 S. K. Pilli, T. E. Furtak, L. D. Brown, T. G. Deutsch, J. A. Turner and A. M. Herring, *Energy Environ. Sci.*, 2011, **4**, 5028.

39 T. Majumder, J. J. L. Hmar, K. Debnath, N. Gogurla, J. N. Roy, S. K. Ray and S. P. Mondal, *J. Appl. Phys.*, 2014, **116**, 34311.

40 A. B. Ellis, S. W. Kaiser, J. M. Bolts and M. S. Wrighton, *J. Am. Chem. Soc.*, 1977, **99**, 2839-2848.

41 Y. Hou, F. Zuo, A. Dagg and P. Feng, *Angew. Chem.*, 2013, **125**, 1286-1290.

42 Q. Liu, H. Lu, Z. Shi, F. Wu, J. Guo, K. Deng and L. Li, *ACS Appl. Mater. Interfaces*, 2014, **6**, 17200-17207.